chemosensors

MDPI

Article

Ag-Functionalized ZIF-8-Derived Porous ZnO Nanocomposites for ppb-Level Acetone Detection

Wenjie Bi [1,2,*], Jinmiao Zhu [1], Bin Zheng [1], Shiwei Yang [1], Chengzhi Ruan [1], Siyu Yu [1], Xinran Li [1], Yinuo Xu [1], Hongyu Yu [1], Yafei Xu [1] and Shantang Liu [3,*]

[1] School of Chemistry and Pharmaceutical Engineering, Hefei Normal University, Hefei 230601, China
[2] Institute of Solid-State Physics, Hefei Institutes of Physical Science, Chinese Academy of Sciences, Hefei 230031, China
[3] Key Laboratory for Green Chemical Process of Ministry of Education, School of Chemistry and Environmental Engineering, Wuhan Institute of Technology, Wuhan 430074, China
* Correspondence: bwj@hfnu.edu.cn (W.B.); stliu@wit.edu.cn (S.L.)

Abstract

In this study, Ag-functionalized porous ZnO nanocomposites were successfully synthesized via pyrolysis of Ag-loaded ZIF-8 precursors. The structural and surface properties of the materials were systematically characterized using XRD, XPS, FESEM, and HRTEM analyses. A gas sensor fabricated from the optimized 3.0 wt% Ag–ZnO sample exhibited a significantly enhanced response (Ra/Rg = 103) toward 100 ppm acetone at an operating temperature of 275 °C, which is approximately 2.51 times greater than that of pristine ZnO. The sensor also demonstrated rapid response/recovery times (6 s/7 s), excellent linearity over a wide concentration range (500 ppb–200 ppm), good selectivity against common interfering VOCs, and stable performance, with over 95% response retention after 30 days. The improved sensing performance is attributed to the hierarchical porous structure derived from ZIF-8 and the increased oxygen vacancy concentration and chemisorbed oxygen species induced by Ag loading, which collectively increase surface reaction activity. This work provides an effective strategy for constructing noble metal-modified porous ZnO materials for sensitive and reliable acetone detection.

Keywords: Ag-loaded ZnO; ZIF-8; MOF-derived porous structure; acetone sensing

1. Introduction

Precise detection of volatile organic compounds (VOCs) is crucial for environmental monitoring, industrial safety, and noninvasive disease diagnosis [1–3]. Among various VOCs, acetone (C_3H_6O) serves not only as a widely used industrial solvent but also as a representative endogenous biomarker associated with human metabolic processes. Clinical studies have indicated that acetone concentrations in the exhaled breath of healthy individuals are typically less than 0.9 ppm, whereas those of diabetic patients are greater than 1.8 ppm [4]. This marked difference highlights acetone as a promising indicator for early diabetes screening and continuous health monitoring. Moreover, the increasingly widespread industrial applications of acetone have raised safety concerns, underscoring the urgent need for high-performance acetone gas sensors [5].

Metal oxide semiconductors (MOSs) have been extensively investigated as gas-sensing materials owing to their low cost, straightforward manufacturing processes, and favorable sensing performance [6,7]. Zinc oxide (ZnO), a representative n-type semiconductor characterized by a wide bandgap (Eg ≈ 3.37 eV), has attracted considerable attention because

Check for updates

Received: 27 February 2026
Revised: 5 April 2026
Accepted: 7 April 2026
Published: 9 April 2026

Copyright: © 2026 by the authors. Licensee MDPI, Basel, Switzerland. This article is an open access article distributed under the terms and conditions of the Creative Commons Attribution (CC BY) license.

of its high electron mobility, diverse nanostructures, and excellent chemical stability [8,9]. However, pristine ZnO sensors still suffer from several intrinsic drawbacks, including a high optimal operating temperature (>300 °C), poor selectivity toward acetone, and strong interference from humidity and other VOCs [10–12]. These limitations significantly restrict their practical application, especially for low-concentration acetone detection in complex environments [13–16].

To overcome these drawbacks, various modification strategies have been proposed, such as noble metal decoration [8,10,16], heterojunction construction [17–19], and morphology engineering [20–22]. Among them, porous metal oxides derived from metal–organic frameworks (MOFs) have recently emerged as promising candidate materials for gas sensing because of their large specific surface area, high porosity, and abundant active sites inherited from MOF precursors [10,12]. Zeolitic imidazolate framework-8 (ZIF-8), composed of Zn^{2+} ions and 2-methylimidazole ligands, stands out because it can serve both as a sacrificial template and as a metal source for preparing porous zinc oxide through pyrolysis [23,24]. In addition, noble metal nanoparticles such as Ag can be introduced into the MOF structure prior to pyrolysis, which enables the formation of uniformly dispersed metal nanoparticles within the resulting metal oxide matrix. It is well established that the presence of Ag can significantly enhance gas sensing performance through catalytic activation of target gas molecules, electron sensitization, and modulation of Schottky barriers at metal–semiconductor interfaces. Furthermore, Ag nanoparticles can promote oxygen absorption and accelerate surface redox reactions, thereby amplifying the resistance changes in the sensing material [21,25,26]. On the basis of these considerations, Ag-modified porous zinc oxide derived from metal–organic frameworks is expected to exhibit synergistically enhanced acetone sensing characteristics because of the integration of the advantages of porous structures and noble metal sensitization. However, systematic investigations regarding the influence of Ag loading on sensing performance and the underlying enhancement mechanisms remain limited.

In this work, ZIF-8 was first synthesized as a precursor and subsequently loaded with Ag nanoparticles via an in situ reduction method. The resulting Ag–ZIF-8 composite was then thermally treated to obtain MOF-derived Ag-modified porous ZnO (Ag–ZnO). The microstructures and surface properties of the samples were systematically characterized, and their acetone sensing performance was comprehensively evaluated. The enhancement mechanism was discussed in terms of the porous structure effect and the catalytic activity of Ag. This study provides an effective strategy for constructing high-performance acetone sensors based on MOF-derived metal oxides and noble metal sensitization.

2. Materials and Methods

2.1. Materials

2-methylimidazole (2-MeIM, AR) and zinc sulfate heptahydrate ($ZnSO_4 \cdot 7H_2O$, AR) were purchased from Macklin Biochemical Co., Ltd. (Shanghai, China). Silver nitrate ($AgNO_3$, AR) was obtained from Sinopharm Chemical Reagent Co., Ltd. (Shanghai, China). Acetone (C_3H_6O, 99.5%) and absolute ethanol (C_2H_5OH, 99.7%) were supplied by Xilong Chemical Company (Shantou, China). Methanol (CH_3OH, 99.5%), Ethylene glycol ($C_2H_6O_2$, 99.5%) and the Formaldehyde solution (CH_2O, 37.0~40.0%) were purchased from Sinopharm Chemical Reagent Co., Ltd. (Shanghai, China). All of the chemical reagents used were of analytical grade and were used directly without further purification.

2.2. Synthesis of ZIF-8 Precursors

ZIF-8 precursors were synthesized via a hydrothermal method. Typically, 0.287 g of $ZnSO_4 \cdot 7H_2O$ and 0.656 g of 2-methylimidazole were separately dissolved in 25 mL

of deionized water to form solutions A and B, respectively. Under magnetic stirring at room temperature, solution A was slowly poured into solution B, and the mixture was continuously stirred for 2 h to ensure a sufficient coordination reaction. The homogeneous mixture was subsequently transferred into a 50 mL Teflon-lined stainless-steel autoclave and heated at 140 °C for 8 h. After naturally cooling to room temperature, the white precipitate was collected by centrifugation, washed repeatedly with deionized water and absolute ethanol to remove residual ions and ligands, and finally dried under a vacuum at 60 °C for 12 h to obtain ZIF-8 powder.

2.3. Preparation of Ag–ZIF-8 Composite Precursors

Ag nanoparticles were introduced onto ZIF-8 via an in situ chemical reduction method. In a typical procedure, 0.5 g of the as-prepared ZIF-8 powder was dispersed in 50 mL of deionized water under ultrasonication for 30 min to obtain a uniform suspension. An aqueous solution containing 0.005 g of $AgNO_3$ (corresponding to a nominal Ag loading of 1 wt%) was subsequently added to the suspension and magnetically stirred for 1 h to facilitate the adsorption of Ag^+ ions onto the ZIF-8 surface. The reaction system was then cooled in an ice-water bath, and a freshly prepared 0.01 M $NaBH_4$ aqueous solution was added dropwise (approximately 1–2 drops per second) under vigorous stirring. During this process, the solution gradually turned grayish-white, accompanied by slight gas evolution, indicating the reduction of Ag+ to metallic Ag nanoparticles and their deposition on the ZIF-8 matrix. After complete addition, the reaction was maintained in an ice bath for another hour to ensure full reduction. The resulting product was collected via centrifugation, washed three times with deionized water and ethanol, and dried at 80 °C for 12 h to obtain the Ag–ZIF-8 composite precursor.

2.4. Pyrolysis and Preparation of Ag–ZnO Series

The MOF-derived Ag-modified porous ZnO materials were obtained by thermal decomposition of the Ag–ZIF-8 precursors. Specifically, the dried Ag–ZIF-8 powder was placed in a ceramic crucible and calcined in a muffle furnace under an air atmosphere. The temperature was increased from room temperature to 500 °C at a heating rate of 2 °C·min^{-1} and maintained for 2 h. After natural cooling, a light gray Ag nanoparticle-decorated porous ZnO composite was obtained, denoted as 1.0 wt% Ag–ZnO. To investigate the influence of Ag loading on the material properties, a series of samples with different Ag contents (0–4 wt%) was prepared by adjusting the amount of $AgNO_3$ during the reduction step. The resulting samples were labeled as pure ZnO, 1.0 wt% Ag–ZnO, 2.0 wt% Ag–ZnO, 3.0 wt% Ag–ZnO and 4.0 wt% Ag–ZnO, respectively. The overall synthesis route of the MOF-derived Ag–ZnO porous composites is schematically illustrated in Figure 1.

2.5. Fabrication and Measurement of Sensors

The fabrication of gas sensors and their gas-sensing performance tests were based on our previously published literature [27,28]. Gas sensors were fabricated using a slurry coating method. First, 5 mg of the sample powder was weighed and dry-ground in an agate mortar for 30 min. Anhydrous ethanol was then added for wet grinding to create a homogeneous slurry. The resulting slurry was uniformly coated onto the surface of a ceramic tube with gold electrodes. After natural drying, the coated tube was annealed at 200 °C for 2 h to enhance the adhesion and structural stability of the sensing film. A nickel-chromium wire (approximately 45 Ω) was subsequently inserted into the ceramic tube as a heating element. The assembled sensor was then aged in an air atmosphere at 300 °C for 7 days to stabilize its electrical properties. A gas-sensing performance test was conducted using a WS-30B gas-sensing test system. The temperature and humidity of the laboratory were controlled at 25 ± 2 °C and 30 ± 5% RH by an air conditioner. The sensor

resistance change was recorded in real time under different concentrations of target gas. Acetone vapor was generated by the static gas distribution method, and its concentration was accurately calculated based on the formula derived from the ideal gas state equation:

$$C = \frac{22.4 \times \rho \times V}{M \times V_c} \quad (1)$$

where C is the target gas concentration (ppm), ρ is the density of liquid acetone (approximately 0.789 g·mL^{-1} at 25 °C), V is the volume of injected liquid acetone (μL), M is the molar mass of acetone (58.08 g·mol^{-1}), Vc is the volume of the test chamber (L), and 22.4 is the molar volume of gas at standard conditions (L·mol^{-1}). The volume of liquid acetone required for the target concentration was calculated by the equation, and then quantitatively injected into the test chamber using a high-precision microinjector (measurement range: 1–10 μL, precision: 0.1 μL).

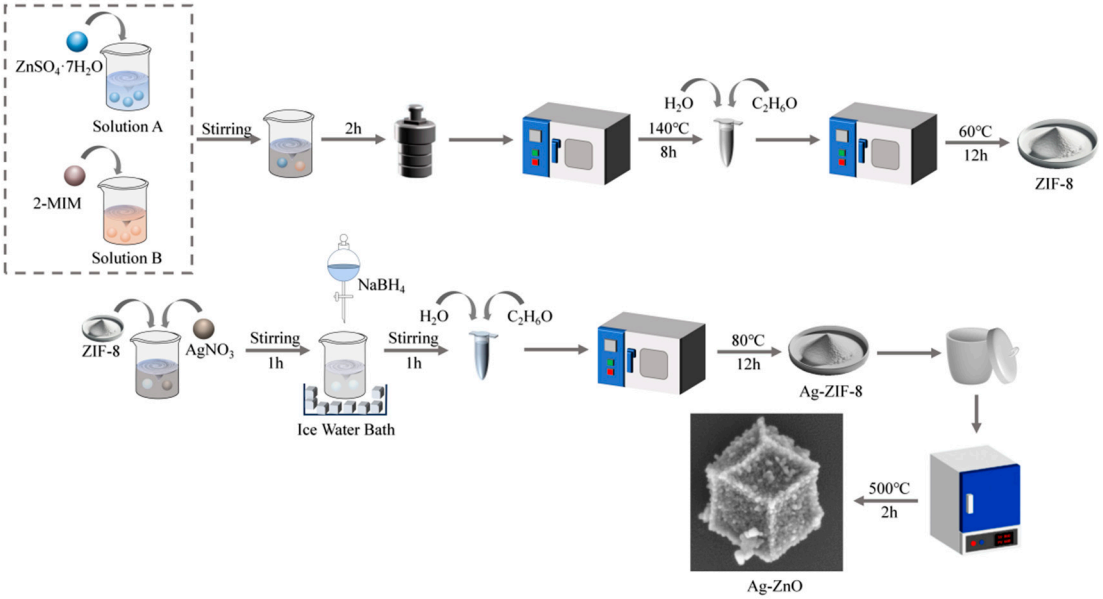

Figure 1. Schematic illustration of the synthesis process of MOF-derived Ag–ZnO porous composites.

For reducing gases, the response S was defined as S = Ra/Rg, where Ra and Rg represent the resistance of the sensor in air and in the target gas, respectively. The response time and recovery time were defined as the time required for the sensor to reach 90% of the total resistance change after the introduction or removal of the target gas. The fabrication process of the sensor is illustrated in Figure 2.

2.6. Characterization

X-ray diffraction patterns were recorded on a Rigaku SmartLab SE diffractometer (Tokyo, Japan) using Cu Kα radiation (λ = 1.5406 Å) at 40 kV and 30 mA. Data were collected in the 2θ range of 10–90° with a scanning rate of 5.0°·min^{-1}. The crystal phases were determined from the peak positions and identified by comparison with the JCPDS database. The surface morphology of the samples was examined using a field-emission SEM (ZEISS Sigma 360, Oberkochen, Germany) operated at an acceleration voltage of 20 kV. The elemental composition and distribution were analyzed by energy-dispersive X-ray spectroscopy (EDS). TEM and HRTEM analyses were performed on an FEI Tecnai F20 microscope (Hillsboro, OR, USA) at 200 kV to observe the particle morphology and lattice structures. XPS measurements were carried out with a Thermo Scientific ESCALAB Xi$^+$ spectrometer (Waltham, MA, USA) using Al Kα radiation (hν = 1486.6 eV). Binding

energies were calibrated using the C 1s peak at 284.8 eV. High-resolution spectra were deconvoluted to analyze the chemical states of surface elements. The specific surface area and pore size distribution of the 3 wt% Ag–ZnO sample were investigated using a surface area analyzer (ASAP2460, Micromeritics, Norcross, GA, USA). Prior to analysis, approximately 0.42 g of the sample was degassed under vacuum at 200 °C for 8 h to remove adsorbed moisture and other contaminants.

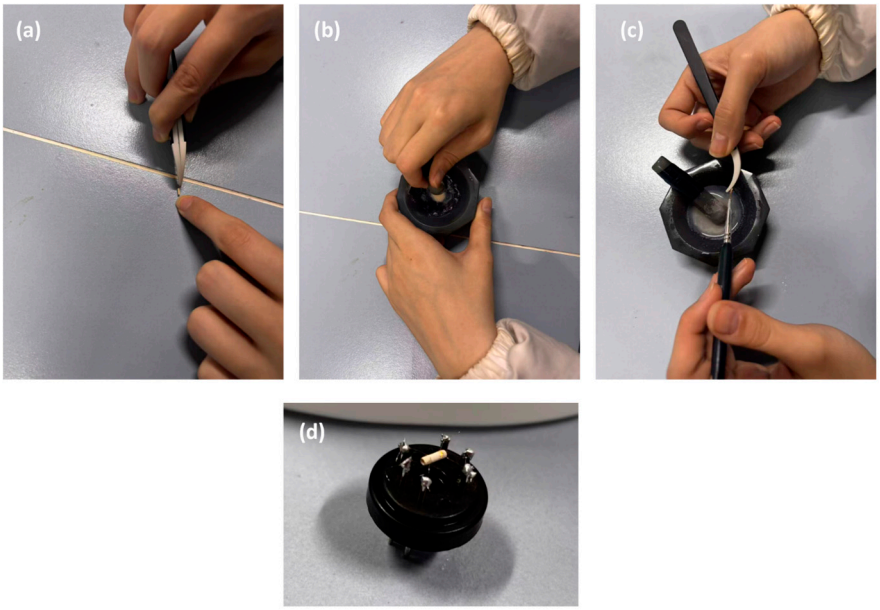

Figure 2. Fabrication process of the gas sensor: (**a**) Lateral electrode configuration; (**b**) Grinding of the paste; (**c**) coating onto a ceramic tube; (**d**) The assembled gas sensor.

3. Results

3.1. Material Characterization

To characterize the crystal structure of the pure ZnO and Ag–ZnO composites with Ag loading amounts of 1.0, 2.0, 3.0, and 4.0 wt%, X-ray diffraction patterns were recorded, as shown in Figure 3. All the samples exhibited distinct diffraction peaks corresponding to the hexagonal wurtzite structure of zinc oxide (JCPDS No. 36-1451), and no impurity phases were detected, confirming that the ZIF-8 precursor was completely converted to crystalline ZnO through thermal decomposition at 500 °C. The characteristic peaks of ZnO appeared at 2θ values of approximately 31.8°, 34.4°, 36.3°, 47.5°, and 56.6°, corresponding to the (100), (002), (101), (102), and (110) crystal planes, respectively, which is consistent with previous reports [29,30]. For the Ag–ZnO composites, no distinct silver characteristic peaks were observed for the 1.0 wt% Ag–ZnO sample. This can be attributed to the low Ag content and the high dispersion of Ag nanoparticles on the zinc oxide surface, which resulted in weak and broad diffraction signals that were partially obscured by the intense ZnO peaks. As the Ag loading increased to 2.0, 3.0, and 4.0 wt%, additional peaks emerged at 2θ ≈ 38.1°, 44.3°, and 64.4°, respectively, corresponding to the (111), (200), and (220) crystal planes of metallic silver (JCPDS No. 04-0784) [31]. The intensity of these diffraction peaks gradually increased with increasing Ag loading, and the peak shapes became sharper. In all the Ag–ZnO samples, no peaks associated with silver oxide (such as Ag_2O or AgO) were detected, confirming that the Ag^+ ions were completely reduced to metallic silver during the synthesis process. The average crystallite size of pure, 1.0 wt%, 2.0 wt%, 3.0 wt% and 4.0 at% Ag–ZnO was calculated using the Scherrer equation, indicating crystallite sizes of 32.7, 24.2, 21.1, 18.5 and 16.9 nm, respectively. Compared with pristine ZnO (32.7 nm), the incorporation of Ag consistently reduces the ZnO crystallite size to the range

of 15–24 nm. This indicates that Ag nanoparticles effectively inhibit ZnO grain growth during the high-temperature pyrolysis of the Ag–ZIF-8 precursor. The smaller crystallite size, combined with the hierarchical porous structure inherited from ZIF-8, contributes to a higher specific surface area and more exposed active sites, which are beneficial for enhancing gas-sensing performance.

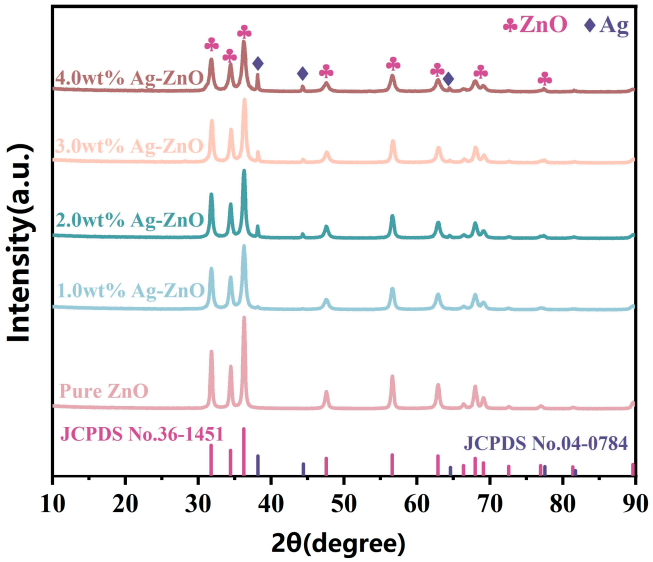

Figure 3. XRD patterns of pure ZnO and Ag–ZnO composites.

The microstructure of the calcined Ag–ZnO composite material was characterized using field emission scanning electron microscopy (FESEM). As shown in Figure 4a–c, the FESEM images of the 3.0 wt% Ag–ZnO sample at different magnifications reveal that the sample has a typical rhombic dodecahedral structure with particle sizes ranging from approximately 200–300 nm. The sample surface is composed of a large number of accumulated nanoparticles and displays a distinctly rough and porous morphology, which is likely attributed to the decomposition of organic ligands during the calcination process and modification by silver nanoparticles. At high magnifications for the SEM images, distinct cavity structures and pores within the particles can be clearly observed. To further elucidate the internal microstructure, the sample was characterized using transmission electron microscopy (TEM). As shown in Figure 4d,e, the sample is composed of numerous primary nanoparticles with sizes ranging from approximately 10 to 30 nm. These particles are interconnected to form a continuous three-dimensional porous network, with abundant pores distributed among the particles, indicating that the material exhibits typical hierarchical porous structure characteristics consistent with the observations from field emission SEM. The high-resolution transmission electron microscopy (HRTEM) image presented in Figure 4f reveals distinct lattice fringes. The region with an interplanar spacing of approximately 0.246 nm corresponds to the (101) plane of ZnO, while lattice fringes with a spacing of approximately 0.237 nm can be identified, which match the (111) plane of metallic Ag, confirming the simultaneous presence of both ZnO and Ag nanoparticles in the sample. Energy-dispersive X-ray spectroscopy (EDS, Figure 4g–j) analysis further confirmed the elemental distribution in the sample. The results show that Zn and O are uniformly distributed throughout the polyhedral framework, whereas Ag nanoparticles are highly dispersed across the entire structure with no obvious agglomeration, indicating good dispersion of Ag nanoparticles within the porous framework.

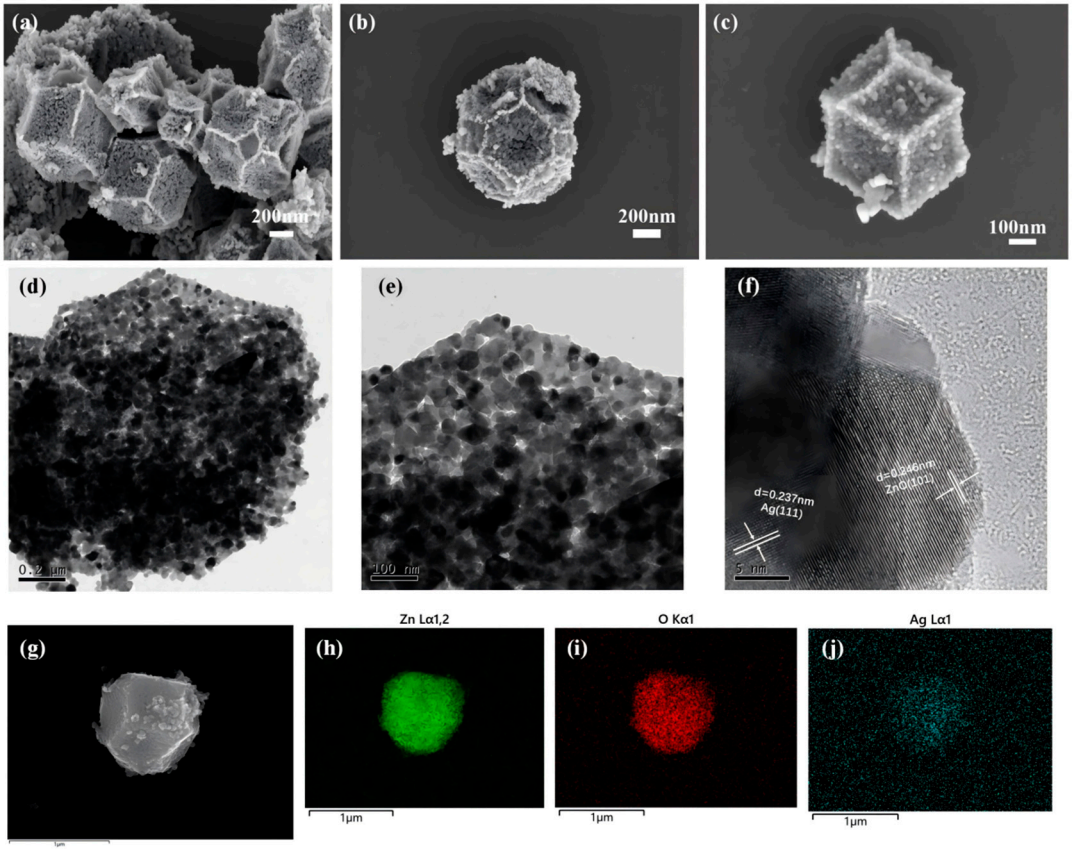

Figure 4. SEM images and TEM images (**a**–**f**) of 3.0 wt% Ag–ZnO; EDS elemental mappings (**g**–**j**) of 3.0 wt% Ag–ZnO.

X-ray photoelectron spectroscopy (XPS) was employed to characterize the chemical composition and valence state characteristics of pure ZnO and 3.0 wt% Ag–ZnO composites, and the results are shown in Figure 5. All binding energy peaks were calibrated using the C 1s peak at 284.6 eV as the reference standard. The XPS survey scans of pure ZnO and the 3.0 wt% Ag–ZnO composite are shown in Figure 5a, where only characteristic peaks of Zn, O, C, and Ag are observed, with no peaks associated with impurity phases detected, confirming the high purity of the prepared samples. Figure 5b displays the high-resolution Zn 2p spectra of the samples, featuring two characteristic peaks at binding energies of approximately 1043.9 eV and 1020.8 eV, which correspond to the Zn $2p_{1/2}$ and Zn $2p_{3/2}$ spin–orbit splitting peaks of Zn^{2+} in ZnO, respectively; the binding energy difference between these peaks is 23.1 eV, which is consistent with the reported characteristic values for ZnO [32,33]. Compared with those for pure ZnO, the Zn 2p peaks for the Ag–ZnO sample exhibit a slight chemical shift (positive shift). This shift can be attributed to the interfacial electron interactions between ZnO and metallic Ag. Owing to the higher work function of Ag, electrons tend to transfer from ZnO to Ag, which reduces the electron density around Zn atoms and thereby increases the binding energy of the inner-shell electrons [34,35]. The high-resolution Ag 3d spectrum of the 3.0 wt% Ag–ZnO composite material is shown in Figure 5c. To elucidate the oxidation states of Ag, the spectrum was deconvoluted into two pairs of peaks. The dominant peaks at 368.4 eV (Ag $3d_5/_2$) and 374.1 eV (Ag $3d_3/_2$) are ascribed to metallic Ag^0, which constitutes the majority of Ag species in the sample. The weaker peaks at 366.8 eV (Ag $3d_5/_2$) and 372.8 eV (Ag $3d_3/_2$) correspond to a small amount of Ag^+, resulting from the mild surface oxidation of Ag nanoparticles during sample handling and air exposure [36]. The spin–orbit splitting energy between Ag $3d_5/_2$ and Ag $3d_3/_2$ is 6.0 eV, indicating that Ag exists in the metallic state (Ag^0) in the composite

material [37]. These results are in excellent agreement with the conclusions of the XRD analysis. The presence of metallic Ag at the Ag/ZnO interface facilitates the formation of a Schottky junction, which is expected to modulate the interfacial charge transfer behavior. To investigate changes in the types and contents of surface oxygen species before and after Ag loading, high-resolution O 1s spectra of pure ZnO and the 3.0 wt% Ag–ZnO composite were analyzed, and the results are shown in Figure 5d. The O 1s peaks of all the samples exhibit asymmetric features and can be deconvoluted into three Gaussian subpeaks: the peak at a binding energy of approximately 529.8 eV is attributed to lattice oxygen (O_L) in the ZnO crystal structure. The binding energy component near 531.3 eV is commonly associated with surface defect-related oxygen species, such as hydroxyl groups (–OH), chemisorbed oxygen, or oxygen in defective environments (O_V). Recent studies suggest that oxygen vacancies do not produce a distinct O 1s signal in this binding energy region; rather, the feature at ~531 eV is more plausibly attributed to surface hydroxylation or adsorbed species, rather than directly to oxygen vacancies. Therefore, in this work, we assign the ~531.3 eV peak to defect-related surface oxygen species without exclusively attributing it to oxygen vacancies. Nevertheless, such surface species are often closely associated with oxygen-deficient environments and can reflect changes in surface defect chemistry [38–40]. The peak at approximately 532.1 eV is assigned to chemisorbed oxygen species (O_C, such as O_2^- and O^-) on the material surface. Quantitative analysis of the relative contents of the three oxygen species reveals that in pure ZnO, the relative contents of O_L, O_V, and O_C are 61.44%, 18.61%, and 19.95%, respectively, whereas in the 3.0 wt% Ag–ZnO composite, the relative contents of O_L, O_V, and O_C are 46.26%, 20.38%, and 33.36%, respectively. According to the literature, the contents of O_V and O_C are closely related to the surface reaction activity of metal oxide materials. After Ag loading, the relative proportions of O_V and O_C in the sample significantly increased, indicating that the surface of the Ag–ZnO composite provides more active reaction sites and an enhanced oxygen adsorption capacity, which in turn promotes improved performance in the gas-sensitive detection field [28].

The porous structure of the 3 wt% Ag–ZnO sample was characterized by N_2 adsorption–desorption measurements, and the results are presented in Figure 6. According to the IUPAC classification, the isotherm exhibits a typical Type IV profile, with a distinct H_3-type hysteresis loop spanning the relative pressure range of 0.4 to 1.0, which is characteristic of mesoporous materials formed by the aggregation of nanoparticles [41]. The gradual increase in N_2 uptake at low to medium relative pressures (P/P_0 = 0.05–0.4) corresponds to monolayer and multilayer adsorption of N_2 molecules on the pore surface, while the steep rise in adsorbed volume at high relative pressures ($P/P_0 > 0.8$) arises from capillary condensation within the mesopores and inter-particle voids. The 3 wt% Ag–ZnO sample showed a BET surface area of 23.20 $m^2\ g^{-1}$ and an average pore diameter of 25.42 nm. The pore size distribution (inset) indicated the presence of mesopores formed by the aggregation of ZnO and Ag nanoparticles, which facilitated efficient gas diffusion and access to active sites for acetone adsorption and reaction. The well-developed mesoporous structure provides abundant pathways for gas transport and sufficient exposed active sites, which is favorable for the enhancement of gas-sensing performance toward acetone.

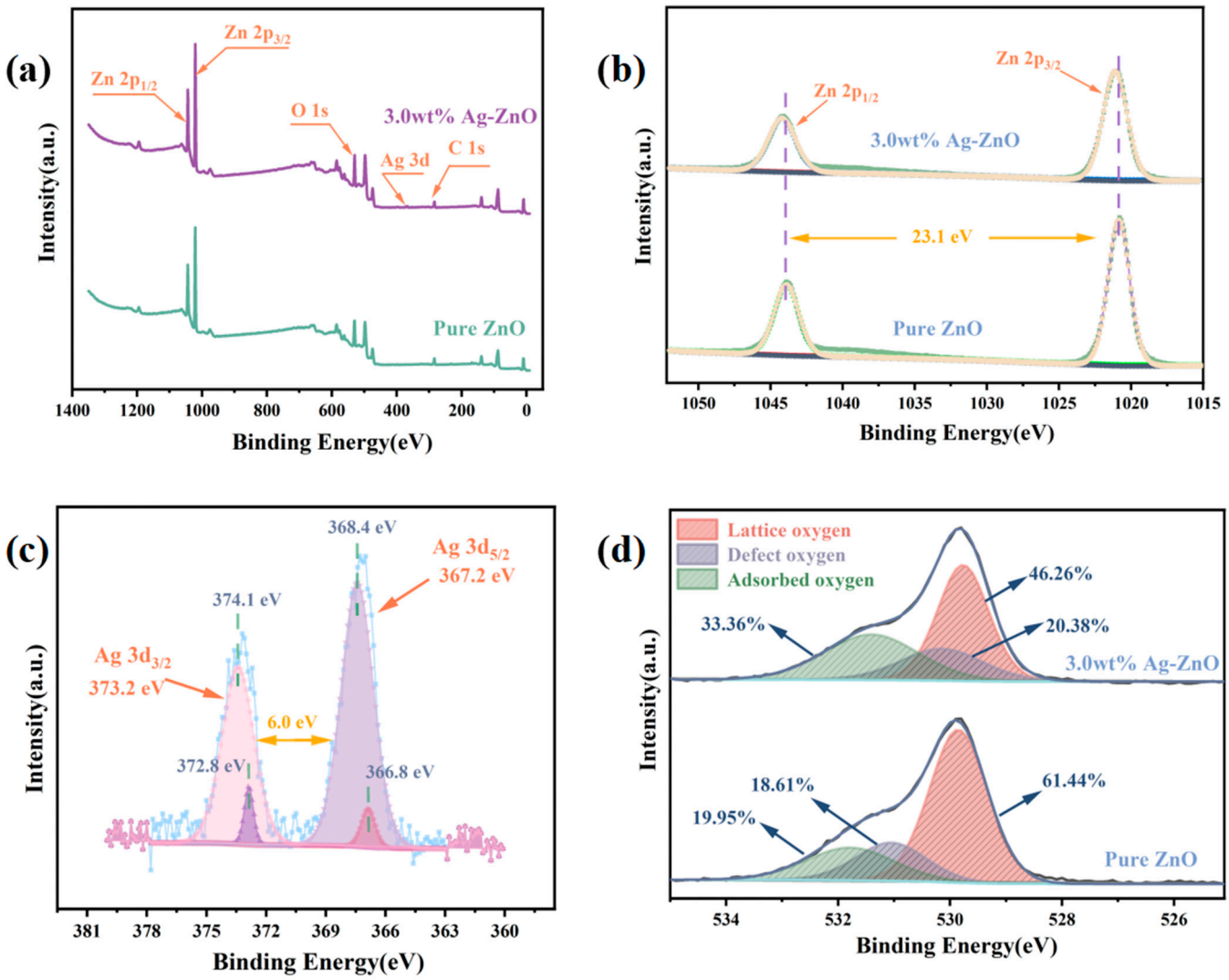

Figure 5. XPS spectra of (**a**) the full survey, (**b**) Zn 2p, (**c**) Ag 3d and (**d**) O 1s.

3.2. Gas Sensing Properties

The operating temperature directly affects the redox reactions on the surface of the sensitive material as well as the rates of gas adsorption and desorption. Therefore, sensors typically exhibit the highest response to the target gas at their optimal operating temperature. To determine the optimal operating temperature of the sensor, the gas-sensing response behaviors of pure ZnO and Ag–ZnO composite materials with different Ag loadings (1.0, 2.0, 3.0, and 4.0 wt%) toward acetone were systematically investigated within the temperature range of 150–325 °C, as shown in Figure 7a. Across the entire testing temperature range, the response values of all the samples first increased but then decreased with increasing temperature, displaying a typical volcano-shaped trend. For the pure ZnO sensor, the response value reached its maximum (approximately 41) at 275 °C. The response value of the Ag nanoparticle-loaded samples increased significantly, with 3.0 wt% Ag–ZnO exhibiting the highest response value of approximately 103 at 275 °C, which is approximately 2.51 times that of pure ZnO. These results indicate that appropriate Ag nanoparticle loading can effectively enhance the gas-sensing performance of ZnO. However, when Ag loading was further increased to 4.0 wt%, the response value decreased, primarily because of the possible shielding of active sites or metal particle agglomeration caused by excessive Ag, which reduced the number of effective reaction sites. In summary,

3.0 wt% was identified as the optimal loading concentration, and 275 °C was identified as the optimal operating temperature.

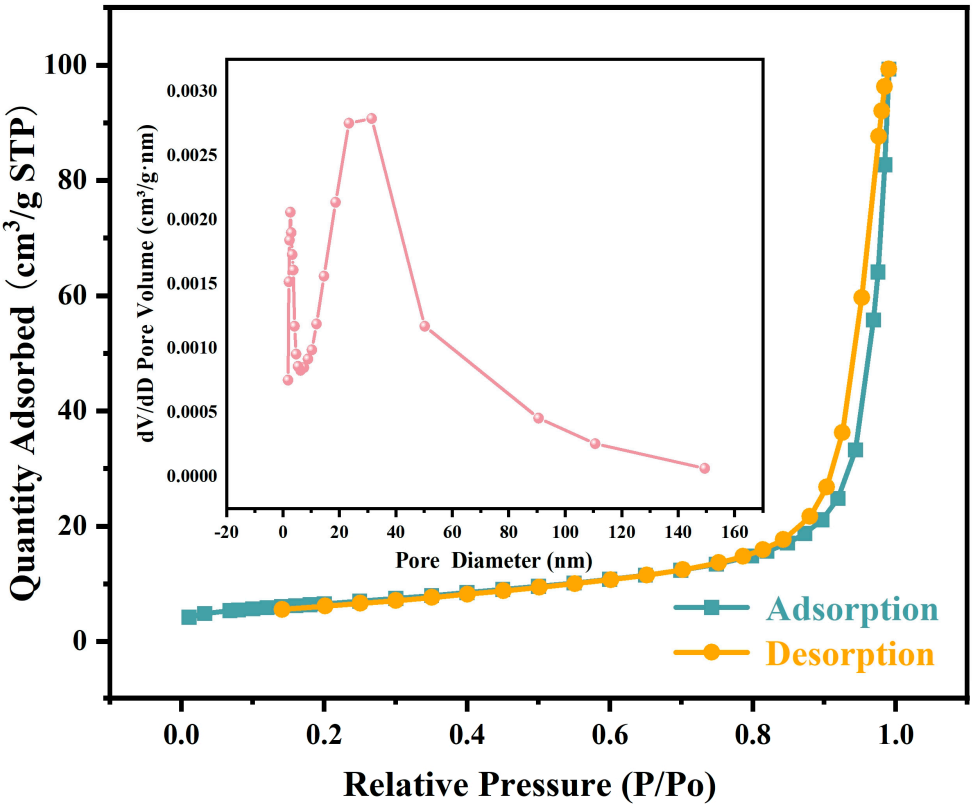

Figure 6. Typical N_2 absorption−desorption isotherms and BJH pore size distribution curves (inset) of 3 wt% Ag−ZnO.

Investigating the response behavior of sensors at different concentrations is highly important for evaluating their detection capability and practical application potential. The dynamic response–recovery curves of the pure ZnO and 3.0 wt% Ag–ZnO sensors toward acetone gas in the concentration range of 500 ppb to 200 ppm are shown in Figure 7b. As shown, both sensors exhibit good repeatability and stable response–recovery characteristics, with the response value gradually increasing as the acetone concentration increases, indicating a clear positive correlation. When the acetone concentration reaches 200 ppm, the response value of pure ZnO is approximately 70, whereas that of 3.0 wt% Ag–ZnO reaches approximately 190, which is approximately 2.7 times greater, further confirming the significant enhancement effect of Ag loading on the gas-sensing performance of ZnO. The inset presents a local magnification of the low-concentration region at 500 ppb and 1 ppm. It can be clearly observed that the sensor still produces stable and distinguishable response signals even at ppb-level concentrations. Specifically, the response value of the 3.0 wt% Ag–ZnO sensor is approximately 1.7 at 500 ppb of acetone and approximately 3.5 at 1 ppm, both of which are significantly greater than of the values for pure ZnO. These results indicate that Ag loading not only enhances the sensor's response intensity in the high-concentration region but also markedly improves its detection capability at low ppb concentrations, demonstrating promising application potential.

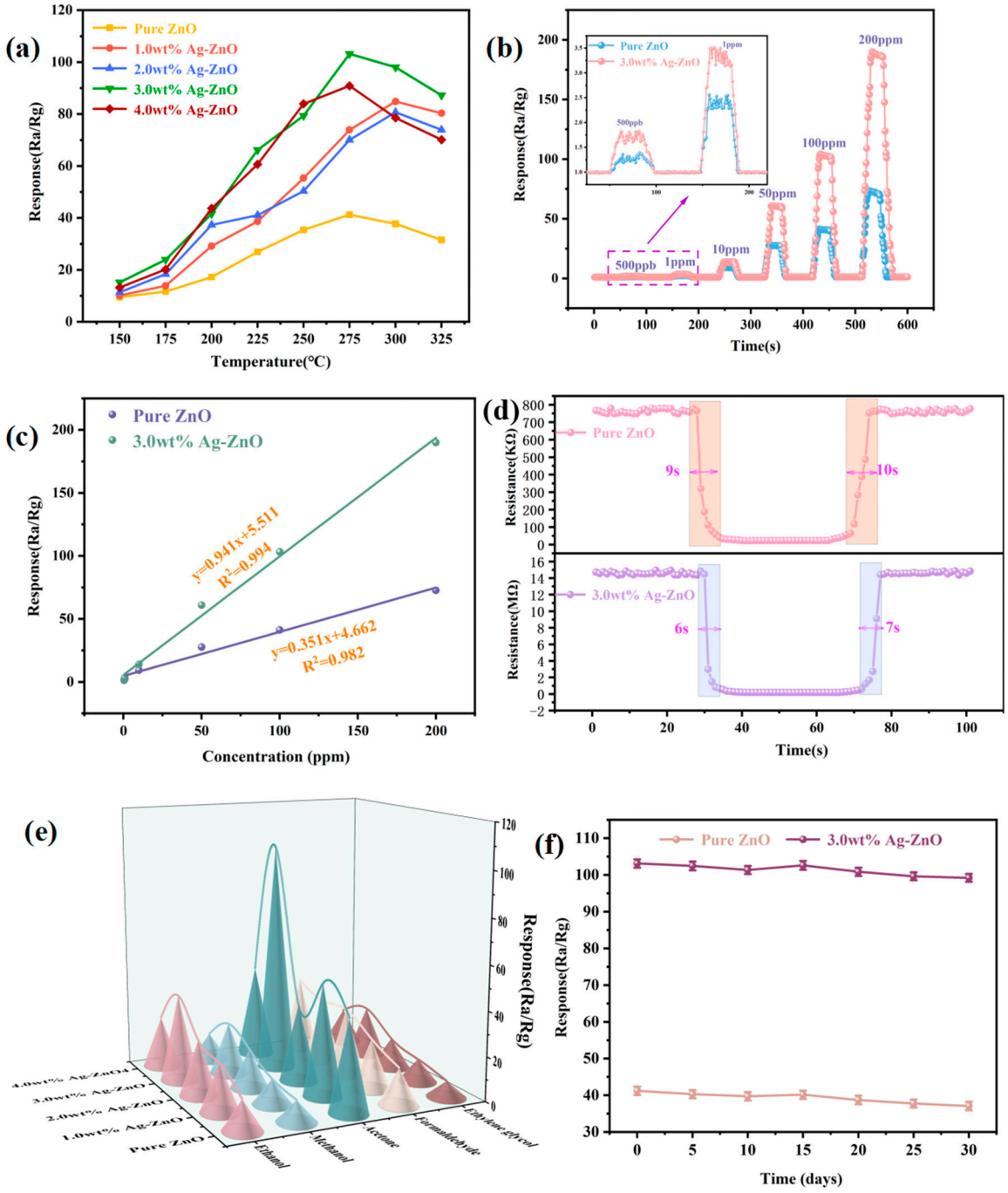

Figure 7. (**a**) Gas sensing performance of samples with different Ag loading ratios toward 100 ppm acetone at different operating temperatures; (**b**) response–recovery curves of all the samples toward acetone from 0.5 to 200 ppm; (**c**) relationship between the response and the acetone concentration; (**d**) dynamic response and recovery curves of pure ZnO and 3.0 wt% Ag–ZnO toward 100 ppm of acetone; (**e**) selectivity of all the samples toward 100 ppm of various gases at their optimal operating temperatures; (**f**) stability of the samples to 100 ppm acetone after 30 days.

Linear fitting analysis was performed to examine the relationship between the response value (Ra/Rg) of the sensor and the acetone concentration within the range of 0.5–200 ppm, as shown in Figure 7c. The coefficient of determination (R^2) for pure ZnO was 0.982, whereas that for 3.0 wt% Ag–ZnO increased to 0.994. A high R^2 value indicates that the Ag-loaded sample maintains a strong linear correlation across the entire concentration range.

The response-recovery time is an important parameter for evaluating the adsorption and desorption rates of gas molecules on the surface of a sensitive material and is crucial

in the real-time monitoring of gases. To further assess the kinetic performance of the sensor, the response–recovery behaviors of pure ZnO and the 3.0 wt% Ag–ZnO sensor were comparatively analyzed, as shown in Figure 7d. The response time and recovery time of the pure ZnO sensor were approximately 9 s and 10 s, respectively, whereas those of the 3.0 wt% Ag–ZnO sensor were reduced to approximately 6 s and 7 s, respectively, demonstrating superior response–recovery performance. This improvement is primarily attributed to the chemical sensitization and spillover effect induced by the uniformly dispersed Ag nanoparticles, which significantly increase the amount of chemically adsorbed oxygen species on the material surface and provide more active sites, thereby accelerating the adsorption and desorption processes of gas molecules.

Selectivity is an important indicator for evaluating the anti-interference ability of sensors in practical applications. In this study, the response selectivities of pure ZnO and Ag–ZnO composites with different Ag loading levels for various volatile organic compounds (VOCs) were systematically evaluated at their respective optimal operating temperatures, with acetone as the target gas and ethanol, methanol, formaldehyde, and ethylene glycol as the interfering gases. The results are presented as a three-dimensional response distribution in Figure 7e. As shown in the figure, compared with the other interfering gases, all the samples exhibited significantly higher response values to acetone, indicating that the prepared materials possessed good selectivity. Among them, the 3.0 wt% Ag–ZnO sample was associated with the highest response value to acetone but maintained relatively low responses to ethanol, methanol, formaldehyde, and ethylene glycol, demonstrating excellent target gas recognition ability. Compared with pure ZnO, Ag-loaded ZnO exhibited an increased difference in response between acetone and interfering gases such as ethanol while maintaining a high response to acetone, indicating that an appropriate level of Ag doping contributes to enhancing the sensor selectivity.

Stability is a key indicator for evaluating a sensor's ability to maintain its performance in actual working environments and serves as an important criterion for assessing the practical application potential of sensors. In this study, a 30-day long-term stability test was conducted on pure ZnO and 3.0 wt% Ag–ZnO sensors at the optimal working temperature. The stability performance was evaluated by monitoring the change in the response to acetone, as shown in Figure 7f. Throughout the entire testing period, neither sensor exhibited significant attenuation in the response value, indicating good stability. Specifically, the response value of the pure ZnO sensor decreased from approximately 41 to approximately 37, whereas that of the 3.0 wt% Ag–ZnO sensor decreased from approximately 103 to approximately 99, indicating only minor fluctuations overall. In contrast, the Ag-loaded sample maintained a relatively high and stable response level throughout the entire testing period, with a response retention rate exceeding 95%, which is highly important for practical application scenarios requiring long-term continuous monitoring.

Table 1 summarizes the performance comparison between the sensors prepared in this study and various acetone sensors reported in the literature. The results indicate that the Ag–ZnO sensor developed in this work maintains a high response value at a relatively low operating temperature, demonstrating excellent gas-sensing performance and promising practical application potential.

Table 1. Comparison of the gas sensing performances of Ag–ZnO-based sensors in acetone.

Materials	T (°C)	Response Time	Recovery Time	Response	Ref.
$ZnO/ZnFe_2O_4$	290	8	32	25.8	[42]
Pt-ZnO-In_2O_3	300	58	1	44	[43]
NiO/ZnO	300	23.5	3	41	[44]

Table 1. *Cont.*

Materials	T (°C)	Response Time	Recovery Time	Response	Ref.
ZnO	300	2	32	6.6	[45]
Ag–ZnO	370	18	10	21	[46]
TiO_2	320	12.3	3	42	[47]
Au@ZnO	300	2	38	37	[48]
Ag–ZnO	275	6	7	105	This work

3.3. Gas Sensing Mechanism

Zinc oxide (ZnO), a typical n-type semiconductor, is widely used in gas sensing, and its gas sensing response originates from resistance modulation and the corresponding change in free carrier concentration caused by surface redox reactions. For n-type ZnO, free electrons in the conduction band are the primary charge carriers. In ambient air, oxygen molecules attach to the ZnO surface through chemical adsorption, extracting free electrons from the conduction band and forming negatively charged oxygen adsorption species. The type of adsorbed oxygen species is strictly dependent on the operating temperature, and its transformation process can be described as follows [28]:

$$O_2(gas) \rightarrow O_2(ads) \quad (2)$$

$$O_2(ads) + e^- \rightarrow O_2^-(ads)\ (T < 100\ ^\circ\mathrm{C}) \quad (3)$$

$$O_2^- + e^- \rightarrow 2O^-(ads)\ (100\ ^\circ\mathrm{C} < T < 300\ ^\circ\mathrm{C}) \quad (4)$$

$$O^-(ads) + e^- \rightarrow O^{2-}(ads)\ (T > 300\ ^\circ\mathrm{C}) \quad (5)$$

Within the operating temperature range relevant to this study, O^- is the dominant and most reactive oxygen species. The extraction of electrons by adsorbed oxygen leads to the formation of an electron depletion layer near the ZnO surface, which increases the baseline resistance of the sensor in air. When exposed to a reducing gas, such as acetone, gas molecules undergo a redox reaction with the adsorbed O^- species, releasing the trapped electrons back into the conduction band:

$$CH_3COCH_3 + 8O^-(ads) \rightarrow 3CO_2 + 3H_2O + 8e^- \quad (6)$$

This reaction decreases the width of the depletion layer and lowers the intergranular barrier, resulting in a proportional decrease in sensor resistance as the acetone concentration increases.

For Ag-loaded ZnO sensors, the significant improvement in gas sensing performance can be attributed to the synergistic enhancement mechanism of electronic sensitization and chemical sensitization. With respect to electronic sensitization, since the work intensity of Ag (~4.7 eV) is slightly higher than that of ZnO (~4.6 eV), electrons spontaneously migrate from ZnO to Ag when the two are in close contact until the Fermi levels reach equilibrium, thereby forming a Schottky barrier at the Ag/ZnO heterojunction interface [49]. This charge transfer process further widens the electron depletion layer on the ZnO surface in air. When exposed to the target gas, the electrons released by the redox reaction can effectively reduce the Schottky barrier height and decrease the depletion layer width, resulting in a significant resistance modulation effect and a substantial increase in the sensing response [50,51].

In terms of chemical sensitization, Ag nanoparticles, which act as highly active catalytic centers, dominate the surface reaction kinetics through the catalytic spillover effect. Ag nanoparticles preferentially adsorb and dissociate oxygen molecules into active atomic oxygen. These activated species subsequently migrate from the Ag surface to adjacent ZnO

regions, which is the spillover effect. This significantly increases the density of chemically adsorbed oxygen available for gas reactions and accelerates the surface redox reaction process. This chemical sensitization further enhances the resistance modulation effect at specific gas concentrations, contributing to improved gas sensing performance [52,53]. XPS analysis provides strong evidence for this effect: the proportion of oxygen vacancies in Ag-loaded ZnO is greater than that in pure ZnO. Oxygen vacancies, which serve as preferential adsorption sites for oxygen molecules, are conducive to the formation of more chemically adsorbed oxygen species. The increased content further enhances the redox reaction capability between the material and the target gas.

In summary, the enhanced gas sensing performance of Ag-loaded ZnO originates from the synergistic enhancement effect of increased oxygen vacancy, the increased chemical adsorption oxygen content, and the surface catalytic effect.

4. Conclusions

A series of MOF-derived Ag–ZnO porous nanocomposites was developed to enhance acetone sensing performance. The integration of hierarchical porosity inherited from ZIF-8 and uniformly distributed Ag nanoparticles significantly improved the surface reactivity and charge modulation capability of ZnO. The optimized 3.0 wt% Ag–ZnO sample exhibited superior sensitivity, wide-range linear detection capability, rapid response dynamics, excellent selectivity, and long-term operational stability. Surface analysis confirmed that Ag loading increased oxygen vacancy and the levels of chemisorbed oxygen species, providing abundant active sites for gas adsorption and reaction. The synergistic coupling between structural porosity and noble metal sensitization offers valuable guidance for interface engineering of MOF-derived semiconductor gas sensors and broadens their potential for practical low-concentration VOC detection.

Author Contributions: Conceptualization: W.B. and S.L.; formal analysis: B.Z., Y.X. (Yinuo Xu), S.Y. (Shiwei Yang), S.Y. (Siyu Yu), C.R., X.L., H.Y. and Y.X. (Yafei Xu); resources: B.Z.; investigation: W.B., C.R., Y.X. (Yafei Xu), X.L., Y.X. (Yinuo Xu), S.Y. (Siyu Yu) and H.Y.; visualization: S.Y. (Siyu Yu); writing—original draft preparation: W.B.; writing—review and editing: S.L., J.Z. and B.Z.; validation: C.R., H.Y. and Y.X. (Yafei Xu); data curation: W.B. and X.L.; supervision: S.Y. (Shiwei Yang); funding acquisition: J.Z.; project administration: J.Z. All authors have read and agreed to the published version of the manuscript.

Funding: This work is financially supported by the Open Funding of Anhui Engineering Laboratory for Medicinal and Food Homologous Natural Resources Exploration (AEL—MFHNRE) (2025KYPT01, 2025KYPT17, 2025KYPT20), the Excellent Talent Foundation of Education Department of Anhui Province (2023AH030097), Jianghuai Talent Training Program, Key Projects of Scientific Re-search Program of Higher Education Institutions in Anhui Province (2024AH051591) and Hefei Normal University 2022 Scientific Research Launch Fund for Introducing High level Talents (No. 2022rcjj35).

Institutional Review Board Statement: Not applicable.

Informed Consent Statement: Not applicable.

Data Availability Statement: Data are contained within the article.

Acknowledgments: The authors would like to thank the Intelligent Micro-Nano and Biomedical Materials Scientific Research Innovation Team (2025KYTD15) for their support in the investigation of this study.

Conflicts of Interest: The authors declare no conflicts of interest.

References

1. Jagan Mohan Reddy, A.; Katari, N.; Nagaraju, P.; Hussain Reddy, K.; Surendra Babu, M. Fabrication and deployment of nanodisc ZnO@ ZIF-8, ZnO@ NA and ZnO@ INA core–shell MOFs: Enhanced NH3 and HCHO gas sensing. *J. Mater. Sci. Mater. Electron.* **2021**, *32*, 7827–7840. [CrossRef]
2. Xu, K.; Wu, K.; Xu, J.; Planche, M.; Deng, S.; Liao, H.; Zhang, C. Metal oxide semiconductor-based heterojunctions synthesized by wet-chemical strategies for efficient volatile organic compounds detection. *Coord. Chem. Rev.* **2025**, *538*, 216735. [CrossRef]
3. Ren, G.; Li, Z.; Yang, W.; Faheem, M.; Xing, J.; Zou, X.; Pan, Q.; Zhu, G.; Du, Y. ZnO@ZIF-8 core-shell microspheres for improved ethanol gas sensing. *Sens. Actuat. B Chem.* **2019**, *284*, 421–427. [CrossRef]
4. Fan, X.; Yang, S.; Huang, C.; Lu, Y.; Dai, P. Preparation and Enhanced Acetone-Sensing Properties of ZIF-8-Derived Co3O4@ZnO Microspheres. *Chemosensors* **2023**, *11*, 376. [CrossRef]
5. Sun, S.; Wang, M.; Chang, X.; Jiang, Y.; Zhang, D.; Wang, D.; Zhang, Y.; Lei, Y. $W_{18}O_{49}/Ti_3C_2T_x$ Mxene nanocomposites for highly sensitive acetone gas sensor with low detection limit. *Sens. Actuat. B Chem.* **2020**, *304*, 127274. [CrossRef]
6. Wang, Y.; Wang, X.; Qi, B.; Cheng, J.; Wang, X.; Shang, Y.; Jia, J. Design of SnO2/ZnO@ZIF-8 Hydrophobic Nanofibers for Improved H2S Gas Sensing. *ChemistrySelect* **2021**, *6*, 5488–5495. [CrossRef]
7. Zhu, L.; Wang, Z.; Wang, J.; Liu, J.; Zhang, J.; Yan, W. Pt-Embedded Metal-Organic Frameworks Deriving Pt/ZnO-In_2O_3 Electrospun Hollow Nanofibers for Enhanced Formaldehyde Gas Sensing. *Chemosensors* **2024**, *12*, 93. [CrossRef]
8. Zhou, T.; Chen, S.; Wang, X.; Xie, C.; Zeng, D. Catalytic Activation of Cobalt Doping Sites in ZIF-71-Coated ZnO Nanorod Arrays for Enhancing Gas-Sensing Performance to Acetone. *ACS Appl. Mater. Interfaces* **2020**, *12*, 48948–48956. [CrossRef] [PubMed]
9. Huang, J.; Zhou, J.; Liu, Z.; Li, X.; Geng, Y.; Tian, X.; Du, Y.; Qian, Z. Enhanced acetone-sensing properties to ppb detection level using Au/Pd-doped ZnO nanorod. *Sens. Actuat. B Chem.* **2020**, *310*, 127129. [CrossRef]
10. Zhang, H.; Guo, S.; Zheng, W.; Wang, H.; Li, H.; Yu, M.; Chang, Z.; Bu, X.; Liu, H. Facile engineering of metal-organic framework derived SnO_2-ZnO composite based gas sensor toward superior acetone sensing performance. *Chem. Eng. J.* **2023**, *469*, 143927. [CrossRef]
11. Yan, W.; Xu, H.; Ling, M.; Zhou, S.; Qiu, T.; Deng, Y.; Zhao, Z.; Zhang, E. MOF-Derived Porous Hollow Co_3O_4@ZnO Cages for High-Performance MEMS Trimethylamine Sensors. *ACS Sens.* **2021**, *6*, 2613–2621. [CrossRef]
12. Zhou, Q.; Xu, L.; Kan, Z.; Yang, L.; Chang, Z.; Dong, B.; Bai, X.; Lu, G.; Song, H. A multi-platform sensor for selective and sensitive H_2S monitoring: Three-dimensional macroporous ZnO encapsulated by MOFs with small Pt nanoparticles. *J. Hazard. Mater.* **2022**, *426*, 128075. [CrossRef]
13. Xiong, Y.; Liu, W.; Qiao, X.; Song, X.; Wang, S.; Zhang, X.; Wang, X.; Tian, J. Confined synthesis of 2D ultrathin ZnO/Co_3O_4 nanomeshes heterostructure for superior triethylamine detection at low temperature. *Sens. Actuat. B Chem.* **2021**, *346*, 130486. [CrossRef]
14. Hussain, S.; Amu-Darko, J.; Wang, M.; Alothman, A.; Ouladsmane, M.; Aldossari, S.; Khan, M.; Qiao, G.; Liu, G. CuO-decorated MOF derived ZnO polyhedral nanostructures for exceptional H_2S gas detection. *Chemosphere* **2023**, *317*, 137827. [CrossRef]
15. Ikram, M.; Lv, H.; Liu, Z.; Shi, K.; Gao, Y. Hydrothermally derived p-n MoS_2-ZnO from p-p MoS_2-ZIF-8 for an efficient detection of NO_2 at room temperature. *J. Mater. Chem. A* **2021**, *9*, 14722–14730. [CrossRef]
16. Amu-Darko, J.; Hussain, S.; Zhang, X.; Alothman, A.; Ouladsmane, M.; Nazir, M.; Qiao, G.; Liu, G. Metal-organic frameworks-derived In_2O_3/ZnO porous hollow nanocages for highly sensitive H_2S gas sensor. *Chemosphere* **2023**, *314*, 137670. [CrossRef] [PubMed]
17. Wang, C.; Peng, M.; Yue, L.; Yang, X.; Zhang, Y. ZIF-8 derived ZnO@CeO_2 heterojunction for ppb-level acetone detection. *Sens. Actuat. A Phys.* **2022**, *342*, 113650. [CrossRef]
18. Song, Y.; Gu, F.; Wang, Z.; Han, D. $ZnFe_2O_4$ Nanoparticles on ZIF-8-Derived ZnO for Enhanced Acetone Sensing. *ACS Appl. Nano Mater.* **2022**, *5*, 15298–15309. [CrossRef]
19. Zhu, Z.; Li, Z.; Xiong, X.; Hu, X.; Wang, X.; Li, N.; Jin, T.; Chen, Y. ZnO/ZnSe heterojunction nanocomposites with oxygen vacancies for acetone sensing. *J. Alloy Compd.* **2022**, *906*, 164316. [CrossRef]
20. Wan, G.; Xue, R.; Qin, T.; Zhang, F.; Li, Y. Acetone detection at low temperature using a gas nano-sensor based on ZnO flakes loaded with metal organic-skeleton ZIF-8. *Mater. Today Commun.* **2023**, *37*, 107561. [CrossRef]
21. Zhang, J.; Liu, J.; Liu, Y.; Li, G.; Guo, J.; Zhang, J.; Zhao, Q.; Che, J.; Li, L.; Gao, J.; et al. Design engineering of MOF-derived ZnO porous nanofibers functionalized with Pt clusters: Significantly improved acetone sensing properties. *Sens. Actuat. B Chem.* **2024**, *400*, 134941. [CrossRef]
22. Qiao, L.; Jia, X.; Zhou, Y.; Yang, J.; Song, H. Highly responsive and selective gas sensors utilizing ZIF-8/porous rGO/ZnO composites. *Sens. Actuat. B Chem.* **2025**, *427*, 137156. [CrossRef]
23. Xian, J.; Li, J.; Wang, W.; Zhu, J.; Li, P.; Leung, C.; Zeng, M.; Lu, X.; Gao, X.; Liu, J. Enhanced specific surface area of ZIF-8 derived ZnO induced by sulfuric acid modification for high-performance acetone gas sensor. *Appl. Surf. Sci.* **2023**, *614*, 156175. [CrossRef]
24. Zhang, Y.; Wang, M.; San, X.; Zhang, L.; Wang, N.; Wang, G.; Meng, D.; Shen, Y. Highly selective gas sensors for formaldehyde detection based on ZnO@ZIF-8 core-shell heterostructures. *Sens. Actuat. B Chem.* **2024**, *398*, 134689. [CrossRef]

25. Lu, Y.; Du, Q.; Yang, L.; Guo, S.; Gao, J.; Hou, M.; Zhang, S.; Zhang, G. Anchoring Pd nanoparticles on metal-organic frameworks for SO_2 detection. *Appl. Surf. Sci.* **2023**, *636*, 157829. [CrossRef]
26. Zhao, F.; Yu, L.; Wang, J.; Cao, W.; Zhang, H.; Wang, H.; Wang, P.; Qiao, Z. Metal-Organic Framework-Derived Au-Doped In_2O_3 Nanotubes for Monitoring CO at the ppb Level. *ACS Sens.* **2024**, *9*, 4007–4016. [CrossRef] [PubMed]
27. Bi, W.; Chen, H.; Yang, S.; Wang, X.; Liu, A.; Ma, X.; Xie, H.; Liu, S. The Three-Dimensional Hierarchical Structure of Bi_x $Sn_{1-x}O_2$ Used for Ultrasensitive Detection of Butanone under UV Irradiation. *ACS Omega* **2024**, *9*, 27932–27944. [CrossRef]
28. Bi, W.; Zhu, J.; Zheng, B.; Liu, S.; Zhang, L. Synthesis of Pd-Doped SnO_2 and Flower-like Hierarchical Structures for Efficient and Rapid Detection of Ethanolamine. *Molecules* **2024**, *29*, 3650. [CrossRef] [PubMed]
29. Ren, H.; Li, W.; Lu, Z.; Huang, J. Enhancing-response acetone gas sensor of porous ZnO/Co_3O_4 heterostructure microspheres with high-content oxygen vacancies. *Ceram. Int.* **2025**, *51*, 48558–48569. [CrossRef]
30. Meng, F.; Li, G.; Ji, H.; Yuan, Z. Investigation on oxygen vacancy regulation mechanism of ZnO gas sensors under temperature modulation mode to distinguish alcohol homologue gases. *Sens. Actuat. B Chem.* **2025**, *423*, 136747. [CrossRef]
31. Liang, Z.; Wang, M.; Zhang, X.; Li, Z.; Du, K.; Yang, J.; Lei, S.; Qiao, G.; Ou, J.; Liu, G. A 2D-0D-2D Sandwich Heterostructure toward High-Performance Room-Temperature Gas Sensing. *ACS Nano* **2024**, *18*, 3669–3680. [CrossRef]
32. Amu-Darko, J.; Hussain, S.; Zhang, X.; Karami, A.; Javed, M.; Yusuf, K.; Manavalan, R.; Wang, M.; Qiao, G.; Liu, G. Enhanced H_2S gas sensing utilizing UV-assisted In_2O_3@ZnO nanosheets. *Ceram. Int.* **2024**, *50*, 38242–38252. [CrossRef]
33. Joshi, N.; da Silva, L.; Jadhav, H.; Shimizu, F.; Suman, P.; M'Peko, J.; Orlandi, M.; Seo, J.; Mastelaro, V.; Oliveira, O. Yolk-shelled $ZnCo_2O_4$ microspheres: Surface properties and gas sensing application. *Sens. Actuat. B Chem.* **2018**, *257*, 906–915. [CrossRef]
34. Torkamani, R.; Aslibeiki, B.; Salari, S.; Azizi, H.; Peddis, D.; Sarkar, T. High-performance hydrogen gas sensor based on Ag-incorporated ZnO nanoparticles. *Sci. Rep.* **2025**, *15*, 38390. [CrossRef] [PubMed]
35. Shen, Z.; Wang, J.; Chiang, W.; Hsiao, C.; Wuu, D.; Chen, G.; Wang, T.; Liu, P.; Chu, J.; Horng, R. Study on performance improvement of zinc oxide gas sensor with silver nanoparticles surface modification. *Sens. Actuat. B Chem.* **2025**, *438*, 137803. [CrossRef]
36. Zhang, X.; Dong, H.; Gu, Z.; Wang, G.; Zuo, Y.; Wang, Y.; Cui, L. Preferential carbon monoxide oxidation on Ag/Al-SBA-15 catalysts: Effect of the Si/Al ratio. *Chem. Eng. J.* **2015**, *269*, 94–104. [CrossRef]
37. Zhu, H.; Haidry, A.; Wang, Z.; Ji, Y. Improved acetone sensing characteristics of TiO_2 nanobelts with Ag modification. *J. Alloy Compd.* **2021**, *887*, 161312. [CrossRef]
38. Idriss, H. On the wrong assignment of the XPS O1s signal at 531–532 eV attributed to oxygen vacancies in photo- and electro-catalysts for water splitting and other materials applications. *Surf. Sci.* **2021**, *712*, 121894. [CrossRef]
39. Graf, A.; Isaacs, M.; Morgan, D. Insight Notes: Considerations in the XPS Analysis of O1s Spectra for Metal Oxides. *Surf. Interface Anal.* **2026**, *58*, 89–95. [CrossRef]
40. Frankcombe, T.; Liu, Y. Interpretation of Oxygen 1s X-ray Photoelectron Spectroscopy of ZnO. *Chem. Mater.* **2023**, *35*, 5468–5474. [CrossRef]
41. Shi, Z.; Xia, L.; Li, G.; Hu, Y. Pt/Au Nanoparticles@Co_3O_4 Cataluminescence Sensor for Rapid Analysis of Methyl Sec-Butyl Ether Impurity in Methyl Tert-Butyl Ether Gasoline Additive. *Chemosensors* **2022**, *10*, 260. [CrossRef]
42. Wang, X.; Zhang, S.; Shao, M.; Huang, J.; Deng, X.; Hou, P.; Xu, X. Fabrication of ZnO/$ZnFe_2O_4$ hollow nanocages through metal organic frameworks route with enhanced gas sensing properties. *Sens. Actuat. B Chem.* **2017**, *251*, 27–33. [CrossRef]
43. Guo, L.; Chen, F.; Xie, N.; Kou, X.; Wang, C.; Sun, Y.; Liu, F.; Liang, X.; Gao, Y.; Yan, X.; et al. Ultra-sensitive sensing platform based on Pt-ZnO-In_2O_3 nanofibers for detection of acetone. *Sens. Actuat. B Chem.* **2018**, *272*, 185–194. [CrossRef]
44. Liu, C.; Wang, B.; Liu, T.; Sun, P.; Gao, Y.; Liu, F.; Lu, G. Facile synthesis and gas sensing properties of the flower-like NiO-decorated ZnO microstructures. *Sens. Actuat. B Chem.* **2016**, *235*, 294–301. [CrossRef]
45. Liu, C.; Zhao, L.; Wang, B.; Sun, P.; Wang, Q.; Gao, Y.; Liang, X.; Zhang, T.; Lu, G. Acetone gas sensor based on NiO/ZnO hollow spheres: Fast response and recovery, and low (ppb) detection limit. *J. Colloid Interface Sci.* **2017**, *495*, 207–215. [CrossRef]
46. Al-Hadeethi, Y.; Umar, A.; Ibrahim, A.; Al-Heniti, S.; Kumar, R.; Baskoutas, S.; Raffah, B. Synthesis, characterization and acetone gas sensing applications of Ag-doped ZnO nanoneedles. *Ceram. Int.* **2017**, *43*, 6765–6770. [CrossRef]
47. Cao, S.; Sui, N.; Zhang, P.; Zhou, T.; Tu, J.; Zhang, T. TiO_2 nanostructures with different crystal phases for sensitive acetone gas sensors. *J. Colloid Interface Sci.* **2022**, *607*, 357–366. [CrossRef]
48. Li, X.; Zhou, X.; Guo, H.; Wang, C.; Liu, J.; Sun, P.; Liu, F.; Lu, G. Design of Au@ZnO Yolk-Shell Nanospheres with Enhanced Gas Sensing Properties. *ACS Appl. Mater. Interfaces* **2014**, *6*, 18661–18667. [CrossRef]
49. Zhang, J.; Lu, H.; Zhang, L.; Leng, D.; Zhang, Y.; Wang, W.; Gao, Y.; Lu, H.; Gao, J.; Zhu, G.; et al. Metal-organic framework-derived ZnO hollow nanocages functionalized with nanoscale Ag catalysts for enhanced ethanol sensing properties. *Sens. Actuat. B Chem.* **2019**, *291*, 458–469. [CrossRef]
50. Navale, S.; Shahbaz, M.; Mirzaei, A.; Kim, S.; Kim, H. Effect of Ag Addition on the Gas-Sensing Properties of Nanostructured Resistive-Based Gas Sensors: An Overview. *Sensors* **2021**, *21*, 6454. [CrossRef] [PubMed]

51. Kaneti, Y.; Zhang, X.; Liu, M.; Yu, D.; Yuan, Y.; Aldous, L.; Jiang, X. Experimental and theoretical studies of gold nanoparticle decorated zinc oxide nanoflakes with exposed {1 0 $\bar{1}$ 0} facets for butylamine sensing. *Sens. Actuat. B Chem.* **2016**, *230*, 581–591. [CrossRef]
52. Liu, L.; Wei, Q.; Yu, X.; Zhang, Y. Metal-Organic Framework-Derived Co_3O_4/Au Heterostructure as a Catalyst for Efficient Oxygen Reduction. *ACS Appl. Mater. Interfaces* **2018**, *10*, 34068–34076. [CrossRef] [PubMed]
53. Yao, R.; Xia, Y.; Yang, L.; Xiang, J.; Zhao, Q.; Guo, S. Noble Metal Functionalized Metal Oxide Semiconductors for Enhanced Gas Sensing. *Molecules* **2025**, *30*, 4683. [CrossRef] [PubMed]

Disclaimer/Publisher's Note: The statements, opinions and data contained in all publications are solely those of the individual author(s) and contributor(s) and not of MDPI and/or the editor(s). MDPI and/or the editor(s) disclaim responsibility for any injury to people or property resulting from any ideas, methods, instructions or products referred to in the content.